

# Ionic Current Rectification through Silica Nanopores

Eduardo R. Cruz-Chu,<sup>†,‡</sup> Aleksei Aksimentiev,<sup>†,§</sup> and Klaus Schulten<sup>\*,†,‡,§</sup>

Beckman Institute for Advanced Science and Technology, Center for Biophysics and Computational Biology, and Department of Physics, University of Illinois at Urbana-Champaign, Urbana, Illinois 61801

Received: May 28, 2008; Revised Manuscript Received: October 20, 2008

Nanopores immersed in electrolytic solution and under the influence of an electric field can produce ionic current rectification, where ionic currents are higher for one voltage polarity than for the opposite polarity, resulting in an asymmetric current–voltage ( $I$ – $V$ ) curve. This behavior has been observed in polymer- and silicon-based nanopores as well as in theoretically studied continuum models. By means of atomic level molecular dynamics (MD) simulations, we have performed a systematic investigation of KCl conductance in silica nanopores with a total simulation time of 680 ns. We found that ion-binding spots at the silica surfaces, such as dangling atoms, have effects on the ion concentration and electrostatic potential inside the nanopore, producing asymmetric  $I$ – $V$  curves. Conversely, silica surfaces without ion-binding spots produce symmetric  $I$ – $V$  curves.

## 1. Introduction

During the past decade, nanotechnology has gained increasing scientific attention due to the development of promising technological tools, such as carbon nanotubes,<sup>1</sup> nanowires,<sup>2</sup> and nanopore sensors.<sup>3</sup> At the same time, nanotechnology has fostered the combination of techniques from different fields, such as ion/electron beam lithography, voltage clamping, and fluorescence spectroscopy, allowing one to craft and study devices with a precision below 100 nm. However, building and controlling such small systems impose many problems. As pointed out by Feynman in 1959,<sup>4</sup> new difficulties arise as devices go down in size. Surface effects, thermal fluctuations, and the discrete nature of matter start to dominate at the nanometer scale, producing phenomena not observed at the microscale. Currently available experimental techniques are not sensitive enough to elucidate the atomic-level dynamics of all these factors, providing many opportunities for theoretical and computational research to complement experiments.<sup>5,6</sup>

Solid-state or synthetic nanopores are among the most popular nanodevices, for example, because of a potential use in low-cost and ultrafast genome sequencing.<sup>7,8</sup> Solid-state nanopores are small pores with nanometer scale radii, made of synthetic materials, such as silica,<sup>9</sup> silicon nitride,<sup>10</sup> or carbon polymers.<sup>11</sup> Immersed in aqueous solution, nanopores can be used as electrical tweezers to study the translocation of charged species, such as ions or nucleic acids.<sup>12–16</sup> Figure 1 shows an atomic-scale model of a silica nanopore. However, nanopore measurements are not yet sensitive enough to resolve DNA sequences with single-base resolution. Even if DNA sequencing remains elusive, synthetic nanopores have already become versatile tools for studying phenomena that can occur in nanoscale confinement,<sup>17</sup> such as electro-osmotic flow<sup>18,19</sup> and streaming currents.<sup>20</sup>

Most applications of nanopores are based on measuring changes in the ionic current. Therefore, understanding ion dynamics through nanopores is desirable. Many interesting

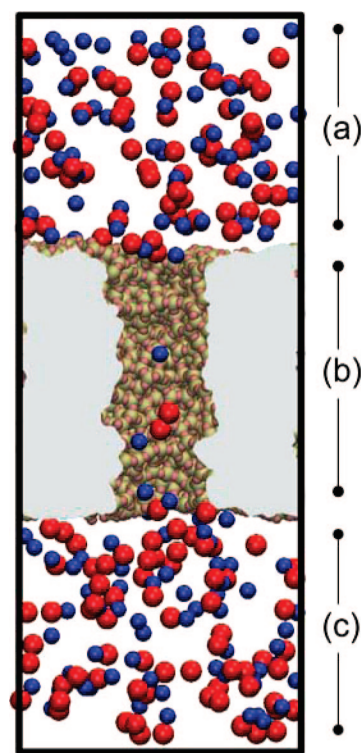


**Figure 1.** Atomic model of a silica nanopore. The figure shows a silica nanopore of 1 nm radius immersed in a KCl solution. The nanopore is shown sliced in the middle. The gray surface covers the bulk silica region, permitting a view of the pore interior.  $K^+$  and  $Cl^-$  ions are pictured in blue and red, respectively. Water molecules are not shown. The system is schematically divided into three regions: cis compartment (a), nanopore region (b), and trans compartment (c).

results that challenge our understanding have been reported, such as ionic current enhancement due to DNA translocation and low salt concentration,<sup>21</sup> conductance–noise variations attributed to nanobubbles,<sup>22</sup> surface charge inversion due to divalent cations,<sup>23,24</sup> increment of resistance induced by  $Ca^{+2}$  ions,<sup>25,26</sup> ion selectivity<sup>27,28</sup> and nanoprecipitation.<sup>29</sup> In this paper, we study the rectification of ionic current in nanopores.

<sup>†</sup> Beckman Institute for Advanced Science and Technology.

<sup>‡</sup> Center for Biophysics and Computational Biology.

<sup>§</sup> Department of Physics.

Under a given voltage, a nanopore produces different ionic currents depending on the polarity of the applied potential, enhancing the ionic current for one polarity but enhancing it less for the same voltage magnitude with opposite polarity. This phenomenon, known as ionic current rectification, has been proposed as the basis for a nanofluidic diode,<sup>30–32</sup> a starting point for developing nanofluidic electronic devices.<sup>33</sup> There has been extensive research on the rectification phenomenon, in particular, for polymer nanopores<sup>34,35</sup> in which case the asymmetric behavior has been attributed to various factors, such as the surface charge, the ionic double layer that fills the entire nanopore space, or an asymmetric electrostatic potential due to structural/chemical asymmetry at the two openings. Several models to explain rectification have been proposed.<sup>36,37</sup> These models were mostly based on continuum macroscopic approaches but were refined to include the peculiarities of the surface system, the latter represented as a continuous surface charge. However, the applicability of continuum descriptions at the scale of a few nanometers is a subject of debate,<sup>28,38,39</sup> since continuum approaches do not take into account the discreteness of the solvent or the influence of the surface topography. Molecular dynamics (MD) simulations can provide a detailed atomistic description of the interactions between the solvated ions and the solid surface, offering a valuable tool for studying the rectification phenomenon. Indeed, MD simulations have already been able to capture the fine effects of surface roughness on ion conduction<sup>40,41</sup> and have been employed to study the interaction of water<sup>42,43</sup> and ions<sup>44,45</sup> with fully hydroxylated silica surfaces. Furthermore, MD simulations have been used to study the interactions between macromolecules and inorganic surfaces in solution.<sup>46,47</sup>

In this paper, we present a systematic study of KCl conductance through silica nanopores having different surface topographies and being built using a silica model designed to mimic the heterogeneity of realistic surfaces.<sup>48</sup> The silica model reproduces the wetting properties of amorphous silica based on the concentration of nonfully coordinated silica atoms, so-called dangling atoms. The definition of a dangling atom is as follows: A silicon and an oxygen atom are considered covalently bonded if they have a separation distance of 2 Å or less; oxygens with fewer than two bonds and silicons with fewer than four bonds are classified as dangling atoms. Below, we report the ionic-current rectification observed in simulated silica nanopores. We then relate the rectification to the atomic events, namely, surface–ion interactions, binding of ions to the solid surface, the electrostatic potential, and the electrostatic force acting inside the pore. Finally, we provide an atomic-level explanation for the observed rectification.

## 2. Methods

In this section, the simulated systems, force fields, simulation conditions, and analysis procedures are presented. To produce amorphous silica pores, we employed the MD programs Cerius<sup>2</sup> v. 4.9<sup>49</sup> and NAMD-lite.<sup>50</sup> The detailed protocols to fabricate atomic-scale models of amorphous silica have been described in detail before<sup>48</sup> and will be summarized below. Ion conduction was investigated using the MD program NAMD 2.6.<sup>51</sup> The results of the simulations were analyzed using custom Matlab<sup>52</sup> routines and VMD<sup>53</sup> scripts.

**2.1. System Setup.** Snapshots of six simulated silica nanopores are shown in Figure 2. Four silica nanopores of 1 nm radius (Figure 2a–d) were considered in this work and classified into three different categories according to the arrangement of surface atoms: crystalline pores, raw cut amorphous pores, and

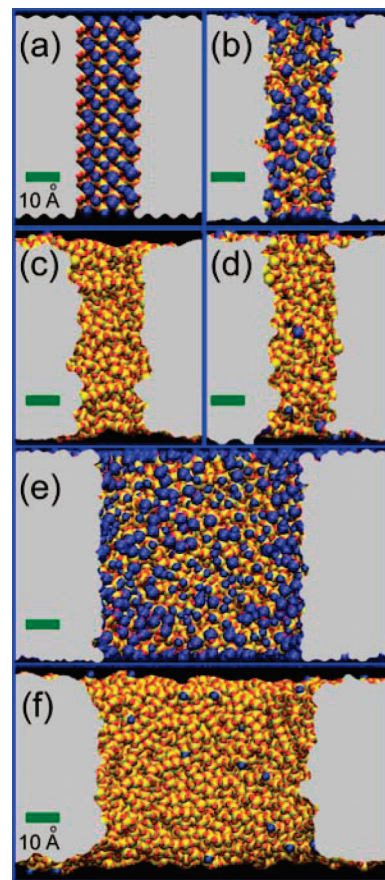


**Figure 2.** Six silica nanopores employed in this study of ionic rectification. Figures show silica systems sliced along the Z axis. Gray surfaces cover the bulk regions; colored beads show the pore surface. Red and yellow beads represent bicoordinated oxygen atoms and four-coordinated silicon atoms, respectively. Blue represents dangling atoms, either dangling oxygen or dangling silicon. Pore A was cut from a crystal structure (a). Pores B and E were cut from amorphous bulk silica (b, e). Pores C, D, and F were obtained after applying annealing cycles (c, d, f) (see Methods). Four pores have 1 nm radius (A–D) and two pores have 3 nm radius (E, F).

annealed amorphous pores. Additionally, two nanopores of 3 nm radius (Figure 2e,f) and two of 1.3 nm radius (Figure 13a,c) were considered.

To create crystalline pores, a silica cube was produced by replicating a cristobalite unit cell, filling a cube with length of 57 Å along each side. Then, the periodicity in the Z axis was removed. One nanopore, called pore A, was built by removing atoms producing a cylindrical pore of 1 nm radius parallel to the Z axis (10368 atoms, Figure 2a).

To create amorphous silica pores, the crystalline silica cube was randomized using an annealing procedure<sup>48</sup> in Cerius<sup>2</sup>. The resulting amorphous bulk had a periodicity of 57 Å × 57 Å × 58 Å. The first raw cut pore of 1 nm radius, called pore B (10488 atoms, Figure 2b), was obtained by removing the periodicity of the amorphous cube along the Z axis and deleting atoms from the center. The second raw cut pore, called pore E (36459 atoms, Figure 2e), was built by replicating the amorphous silica bulk 2 × 2 along the X and Y axes to accommodate a cylindrical pore of 3 nm radius. To preserve electroneutrality, we enforced a ratio of two oxygen atoms per one silicon atom by removing a few extra atoms from the surfaces.

Annealed pores were created by applying simulated annealing procedures to pore B<sup>48</sup> using two silica force fields: GLASSFF\_1.01 and GLASSFF\_2.01. The GLASSFF\_2.01 force field

TABLE 1: Summary of MD Simulations<sup>a</sup>

nanopore	radius (nm)	[KCl] (M)	voltage (V)	time (ns)
A, B, C, D	1.0	1	$\pm 0.12, \pm 0.24, \pm 0.50, \pm 1.00, \pm 2.00$	10 each run
		0	$\pm 1.00$	10 each run
C1, C2	1.3	1	$\pm 1.00$	30 each run
E, F	3.0	1	$\pm 1.00$	10 each run
B, C	1.0	single K <sup>+</sup>	-1	16 for B, 8 for C
		single Cl <sup>-</sup>	+1	8 each run

<sup>a</sup> After energy minimization for 400 steps and equilibration for 1 ns, the systems were simulated under the specified voltage biases.

is composed of a repulsive van der Waals term, a screened electrostatic Coulomb term, and a three-body nonbonded potential that introduces an energetic bias toward tetrahedral arrangement of silica glass. GLASSFF\_1.01 is an earlier version of GLASSFF\_2.01 without the three-body term. Therefore, the GLASSFF\_1.01 force field allows larger distortions from the tetrahedral arrangement, which is needed to obtain a surface of silica without dangling atoms. Two annealed pores were produced, namely, pore C (Figure 2c) and pore D (Figure 2d), annealed with GLASSFF\_1.01 and GLASSFF\_2.01, respectively. The third annealed pore, pore F (Figure 2f), was created by annealing pore E using the BKS force field<sup>54</sup> and NAMD-lite.<sup>50</sup> The BKS force field involves a Buckingham potential and a Coulombic term; this force field has been extensively validated for amorphous silica structures. It was used instead of GLASSFF\_1.01 due to the increased computational performance of NAMD-lite over Cerius<sup>2</sup> to anneal a structure of 36459 atoms. Finally, we used annealed pore C, which has a negligible number of dangling atoms, as a template to produce two nanopores of 1.3 nm radius, called C1 (9,756 atoms, Figure 13a) and C2 (9753 atoms, Figure 13e). By removing silica atoms from the center of pore C, it is possible to obtain nanopores that expose raw cut amorphous surface in the nanopore region, while keeping annealed surfaces in contact with the solvent compartments. Such pores were designed to study the ion conduction observed in raw cut amorphous pores and will be presented at the end of the Results and Discussion section.

To solvate the silica nanopores, rectangular water boxes were generated using the *Solvate* plugin of VMD<sup>53</sup> and placed above and below the silica nanopores. The dimensions of the water boxes match the *X* and *Y* periodic lattice vectors of the silica nanopores and have 60 Å length along the *Z* axis. To induce water permeation, the systems were energy minimized for 400 steps using the conjugate gradient method and then equilibrated for 1 ns of molecular dynamics (MD) simulation (see detailed MD protocol below). Subsequently, the VMD plug-in *Autoionize* was used to place ions randomly, corresponding to 1 M KCl concentration. The systems were then energy minimized (400 steps) and equilibrated for 1 ns. The last frames of the equilibration simulations were used to study ion conduction. The final systems composed of silica, water, and ions are periodic, with unit cell dimensions of 55 Å × 55 Å × 165 Å for pore A, 57 Å × 57 Å × 150 Å for pores B, C, and D, 57 Å × 57 Å × 146 Å for pores C1 and C2, and 110 Å × 110 Å × 160 Å for pores E and F. The systems were simulated under different voltage biases. The voltage signs are defined relative to the cis solvent compartment (see Figure 1). A positive voltage bias induces cations to move from the trans solvent compartment to the cis solvent compartment.

Table 1 summarizes all simulations performed. For the present study we carried out 680 ns of MD simulations. The extensive

simulations are feasible due to the excellent efficiency and scalability of NAMD 2.6.<sup>51</sup> Simulated systems composed of silica, water, and ions comprise 46000 atoms, except for systems with 3 nm radius pores (E and F) that comprise 193000 atoms. The different silica pores simulated and voltages applied offer a wide sample of ionic current characteristics.

**2.2. Molecular Dynamics.** To simulate systems composed of silica, water, and ions we employed the program NAMD 2.6.<sup>51</sup> Silica parameters were taken from our custom silica force field, which reproduces the wetting properties of amorphous silica.<sup>48</sup> Parameters for ions were taken from the CHARMM force field,<sup>55</sup> the TIP3P<sup>56</sup> model being used for water. All simulations were performed under periodic boundary conditions with 1 fs time step. Van der Waals interactions were computed using a cutoff distance of 12 Å with a switching function starting at 10 Å, whereas long-range electrostatic forces were calculated using the particle-mesh Ewald method, with a grid density of 1/Å<sup>3</sup>. A multiple time stepping procedure<sup>57,58</sup> was employed to calculate bonded and nonbonded interactions. The temperature of the systems was maintained at 300 K using a Langevin thermostat. Simulations were performed in the *NpT* ensemble using a hybrid Nosé-Hoover Langevin piston<sup>59</sup> to maintain a pressure of 1 atm. All silica atoms were restrained to their original positions using a harmonic force with a spring constant of 5 (kcal/mol)/Å<sup>2</sup>, while water molecules and ions were allowed to move freely. To induce ionic current through the nanopore, a uniform electrostatic field  $E_z$  was applied to all atoms in the *Z* direction.<sup>12,60</sup> The voltage bias  $\varepsilon$  across the simulated system is

$$\varepsilon = -L_z E_z \quad (1)$$

where  $L_z$  is the length of the periodic system along the *Z* axis. Different voltage biases were applied ranging from -2 to +2 V (see Table 1). Coordinates of all atoms were saved every picosecond for later analysis.

To study the effect of the silica surface on the ion dynamics without the influence of colliding ions, four *single ion* simulations were performed. A single ion, either K<sup>+</sup> or Cl<sup>-</sup>, was placed in the cis compartment, 40 Å above the top surface of pores B and C. To induce translocation from the cis to the trans compartment, the systems were simulated under a voltage of +1 V for a Cl<sup>-</sup> ion and -1 V for a K<sup>+</sup> ion. To avoid the ion diffusing away from the nanopore opening, the ion movement was limited to a cylinder of 15 Å radius and 140 Å length concentric with the pore axis, using a phantom surface<sup>61,62</sup> that imposes boundary limits on the ion, while allowing water molecules to diffuse freely. When the ion reaches the phantom surface, it experiences an elastic collision that pushes it back toward the interior of the cylinder. The phantom surfaces were implemented using the *Tcl Forces* feature available in NAMD<sup>51</sup> and were computed every 10 fs. To maintain electroneutrality, a counterion was located 40 Å below the bottom pore surface and 10 Å away from the phantom surface; the counterion was restrained to its original position using a harmonic force with a spring constant of 5 (kcal/mol)/Å<sup>2</sup>.

**2.3. Analysis. Ionic Current.** In order to study the current-voltage characteristics of the nanopore, we computed the instantaneous ionic currents through the pore,  $I(t)$ , using<sup>12</sup>

$$I(t) = \frac{1}{\Delta t L_z} \sum_{i=1}^N q_i (z_i(t + \Delta t) - z_i(t)) \quad (2)$$

where  $q_i$  is the charge of ion  $i$ ,  $z_i$  is the *Z* coordinate,  $L_z$  is the length of the elementary cell along the *Z* axis, and  $\Delta t$  is the time between trajectory frames, namely, 1 ps. Nonannealed



pores (A, B, and E) require from 2 to 5 ns to reach a steady-state current, depending on the applied voltage. Therefore, the ionic currents reported later are average values of the last 4 ns of each 10 ns trajectory. For pores C1 and C2, the average ionic currents were calculated over the last 20 ns of each 30 ns trajectory. The standard error of the ionic current was computed using  $\sigma/\sqrt{n}$ , where  $n$  is the number of ps used for calculating the average current and  $\sigma$  is the standard deviation.

**Radial Ionic Concentration.** In order to investigate the ion distribution inside the nanopores and near the nanopore wall, we calculated the ion concentration as a function of radial distance from the pore center. For that purpose, we average the ion concentration over cylindrical rings concentric with the pore axis, each ring with 44 Å height and of 1 Å width from the inner to the outer boundary. Starting from the center of the pore, the inner boundary of each ring was displaced by 0.2 Å in the radial direction, up to reaching the nanopore wall. The radial concentrations reported below are average values over the last 4 ns of each simulation.

**Residence Time.** During the course of the simulations, we observed temporal adsorption of ions to the silica surface. To study the ion-adsorption process, we calculated the residence time of the ions in contact with the surface. For these calculations, the entire silica surface was considered, not only the exposed surface in the nanopore region but also those of cis and trans compartments. The residence time was computed by counting the time an ion spends in contact with the surface. An ion was considered in contact with the surface if the distance between the centers of the ion and the nearest silica atom was less than 5 Å. When an ion left that region and then returned, it was counted as a different ion.

**Electrostatic potential.** The ionic current is affected not only by the external applied potential but also by the electrostatic potential generated by the location of all charged species in the system, such as silica, ions, and water. To investigate how these potentials alter the ionic current, we computed  $V_{\text{mean}}^{\varepsilon}$ , the mean electrostatic potential at voltage  $\varepsilon$ , defined through

$$V_{\text{mean}}^{\varepsilon}(\mathbf{r}) = \langle V_{\text{intr}}(\mathbf{r}) + V_{\text{appl}}^{\varepsilon}(\mathbf{r}) \rangle_{4\text{ns}} \quad (3)$$

$V_{\text{intr}}(\mathbf{r})$  refers to the intrinsic electrostatic potential determined by the location of all charged atoms and has been computed with the VMD plugin *PMEpot* which employs for the purpose a modified version of the PME method.<sup>63</sup> The details of our procedure are described elsewhere.<sup>64</sup>  $V_{\text{appl}}^{\varepsilon}(\mathbf{r})$  refers to the external, i.e., applied, potential defined through

$$V_{\text{appl}}^{\varepsilon}(\mathbf{r}) = -\varepsilon \cdot [Z - Z_{\text{min}}] \quad (4)$$

where  $\varepsilon$  is the voltage bias (eq 1) and  $Z_{\text{min}}$  is the beginning of the periodic cell along the  $Z$  axis. Note that  $V_{\text{appl}}^{\varepsilon}(\mathbf{r})$  depends only on the  $Z$  coordinate. Equation 3 states that  $V_{\text{mean}}^{\varepsilon}(\mathbf{r})$  is an average (denoted by  $\langle \cdot \cdot \cdot \rangle_{4\text{ns}}$ ) over the last 4 ns of each MD simulation.

$V_{\text{mean}}^{\varepsilon}(\mathbf{r})$  describes the mean electrostatic potential for every point  $\mathbf{r}$  in the simulation space. However, of main interest is the variation of the average potential along the pore axis, i.e., along the  $Z$  axis. The associated potential, denoted by  $V_{\text{fit}}^{\varepsilon}(Z)$ , has been calculated by determining first the average potential along the  $Z$  axis

$$V_{\text{avg}}^{\varepsilon}(Z) = \langle V_{\text{mean}}^{\varepsilon}(r) \rangle_{\text{cylinder along } Z \text{ axis}} \quad (5)$$

where  $\langle \cdot \cdot \cdot \rangle_{\text{cylinder along } Z \text{ axis}}$  denotes the average of  $V_{\text{mean}}^{\varepsilon}(\mathbf{r})$  over cylinders concentric with the pore axis, each cylinder of 1 Å height and 3 Å radius centered at  $Z$ . The radius of 3 Å was

chosen to avoid distortions of the potential due to the silica wall.  $V_{\text{fit}}^{\varepsilon}(Z)$  was assumed to adopt the analytical function

$$V_{\text{fit}}^{\varepsilon}(Z) = \frac{\varepsilon}{\pi} \arctan(-b[Z - Z_0]), \quad (6)$$

where  $b$  and  $Z_0$  are fitting parameters determined through matching  $V_{\text{fit}}^{\varepsilon}(Z)$  to  $V_{\text{avg}}^{\varepsilon}(Z)$ .  $V_{\text{fit}}^{\varepsilon}(Z)$  is a smooth differentiable function that represents the key variation of the electrostatic potential along the continuous  $Z$  axis at  $\varepsilon$  bias.<sup>62</sup>

In order to study the electrostatic contribution of all charged species in the system discounting the influence of  $V_{\text{appl}}$ , we introduced the potential

$$V_{\text{syst}}(Z) = \frac{1}{2} \cdot [V_{\text{fit}}^{+1V}(Z) + V_{\text{fit}}^{-1V}(Z)] \quad (7)$$

where  $V_{\text{fit}}^{+1V}(Z)$  and  $V_{\text{fit}}^{-1V}(Z)$  correspond to  $V_{\text{fit}}^{\varepsilon}(Z)$  at +1 and −1 V biases, respectively.  $V_{\text{syst}}(Z)$  cancels out the effect of the applied potential and reflects only the intrinsic electrostatic contribution of the system.

**Single Ion Simulations.** In case of our *single ion* simulations, we were interested in calculating the potential energy,  $U$ , acting on a single ion and differentiating the contribution of the ion–silica energy from the ion–water energy. The intermolecular potential energies were calculated using the *NAMD Energy*<sup>65</sup> plugin provided with VMD.<sup>53</sup> *NAMD Energy* computes the potential energy for each frame of a given trajectory, but only considering two selected groups of atoms. In this case, the *single ion* simulations described above provided the trajectories. The intermolecular energies were calculated on two different selections, ion–silica and ion–water. Van der Waals and electrostatic interactions were computed using a cutoff of 12 Å with a switching function starting at 10 Å.

### 3. Results and Discussion

In the following, we present and discuss the results of our simulations. First, we calculate the ionic current and describe the pores that produce ionic rectification. Then, we focus on ion binding on nonannealed surfaces and investigate the main factors responsible for the binding. Finally, we compute the electrostatic potential and interactions for different silica nanopores and relate the ionic currents seen in our simulations to the surface characteristics of nanopores.

Simulations lasting altogether 480 ns have been performed for silica pores A, B, C, and D. As described above, these are cylindrical pores that differ in their arrangement of surface atoms. Their 1 nm pore radii are small enough to capture ion–silica interactions mediated by the solvent and avoid ion bulklike behavior in the interior of the pore.<sup>66,67</sup> To characterize the current–voltage dependence, we tested 10 voltage biases (Table 1).

**3.1. Ionic Current.** Silicon-based nanopores can produce linear ohmic responses;<sup>10,12,68</sup> however, ionic current rectification is not unusual. The presence of rectification has been reported in  $\text{Si}_3\text{N}_4$  nanopores coated with  $\text{SiO}_2$ <sup>69</sup> and glass nanopipets.<sup>70</sup> In the respective studies, ionic rectification can be abolished either by lowering the pH to neutralize the surface charge or by coating the surface with  $\text{Al}_2\text{O}_3$ , showing the dependence of rectification on the physical characteristics of the nanopore surface.

Figure 3 presents the  $I$ – $V$  curves for pores A, B, C, and D. In general, our simulations provide a good qualitative description of observed ionic current behavior. For example, for  $\text{Si}_3\text{N}_4$  pores of 1 nm radius, the experimental ionic conductance has been estimated to be 1.09 nS<sup>10</sup> (or 1.09 nA at 1 V assuming a linear

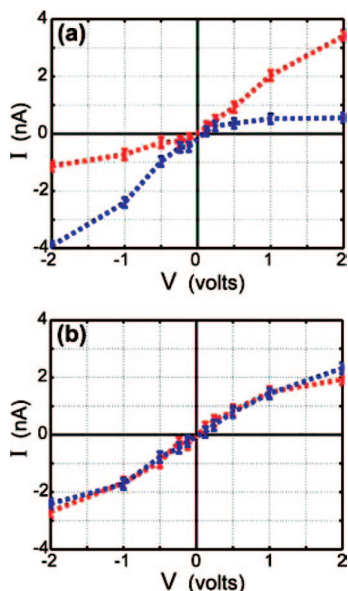


**Figure 3.**  $I$ – $V$  curve for 1 nm radius pores immersed in 1 M KCl. Panel a shows the  $I$ – $V$  curves for pores A (blue) and B (red), both pores producing rectification. Panel b shows the  $I$ – $V$  curves for pores C (red) and D (blue), both pores producing a symmetric curve, i.e., no rectification. Error bars show the standard error, defined as  $\sigma/\sqrt{n}$ , where  $\sigma$  is the standard deviation and  $n$  is the number of MD frames used for calculating the average, namely, 4000.

response), which compares well with our results. One cannot expect, though, quantitative agreement between measured and simulated  $I$ – $V$  characteristics. Even though MD simulations provide a detailed atomic description, there are inherent discrepancies between the MD model and the real physical system, such as membrane thickness, surface charge, and time scale of measurements.<sup>12</sup> The silica surfaces used are approximate models that reproduce wettability and surface topography quite accurately but do not reproduce other physical features equally well. For instance, our model employs the same set of partial charges for dangling and bulk atoms; a more accurate representation would include different partial charges based on the connectivity and local environment of the dangling atoms.<sup>71</sup> The polarizability of silica has not been taken into account either.<sup>72</sup> Furthermore, the varying properties of our surfaces are due to the presence of defects on the surface, such as dangling atoms, and not to explicit deprotonated silanols. We note that a variety of defects have been extensively reported in the literature,<sup>73</sup> such as defects produced when the silica surface is damaged by mechanical stress<sup>74</sup> or by ion and electron beams.<sup>75,76</sup> One indeed expects that such defects, in contact with water, would produce deprotonated silanols. Unfortunately, silica models that reproduce all such surface defects in detail and can be used with the TIP3P water model are not yet available. Recent work focused on fully hydroxylated silica models,<sup>44,45</sup> which are inadequate at neutral pH conditions. A most recent publication has used a model of deprotonated silanol.<sup>24</sup> Nevertheless, the integration of silica models and MD models employed in biomolecular simulations is at an early stage of development and there is still much need for improvement.

Figure 3 shows that the  $I$ – $V$  curve depends strongly on the type of pore employed. Pores A and B (Figure 3a) show an asymmetric  $I$ – $V$  curve with a clear hindrance in the ion conduction for positive and for negative biases, respectively. At low biases ( $\pm 0.125$  and  $\pm 0.25$  V) the magnitudes of the current do not show any significant rectification. However, at higher biases ( $\pm 0.5$ ,  $\pm 1$ , and  $\pm 2$  V), rectification arises and

**TABLE 2: Rectification Factor ( $f_{\text{rec}}$ ) and Number of Ions inside Pores A, B, C, D, E, and F<sup>a</sup>**

nanopore	$f_{\text{rec}}$	number of ions inside the pore			
		+1 V		–1 V	
		K <sup>+</sup>	Cl <sup>–</sup>	K <sup>+</sup>	Cl <sup>–</sup>
A	$4.60 \pm 1.46$	$8.5 \pm 1.0$	$1.3 \pm 0.5$	$24.5 \pm 1.8$	$14.1 \pm 1.8$
B	$0.36 \pm 0.09$	$17.4 \pm 1.7$	$15.8 \pm 1.9$	$5.6 \pm 1.1$	$4.2 \pm 1.4$
C	$1.13 \pm 0.19$	$4.7 \pm 1.4$	$5.0 \pm 1.2$	$5.7 \pm 1.0$	$6.2 \pm 1.2$
D	$1.20 \pm 0.20$	$7.1 \pm 1.5$	$5.9 \pm 1.4$	$5.8 \pm 1.5$	$5.7 \pm 1.6$
E	$0.85 \pm 0.02$	$91.9 \pm 2.8$	$85.3 \pm 3.3$	$69.7 \pm 6.1$	$59.8 \pm 4.9$
F	$0.95 \pm 0.02$	$74.4 \pm 3.8$	$72.7 \pm 4.3$	$68.1 \pm 3.8$	$67.8 \pm 4.1$

<sup>a</sup> Nanopores are listed in the first column.  $f_{\text{rec}} \pm$  its standard error are shown in the second column and was calculated using eq 8. The average number of ions  $\pm$  its standard deviation are shown in the next columns, for K<sup>+</sup> and Cl<sup>–</sup> ions under +1 V bias (third and fourth column), as well as under –1 V bias (fifth and sixth column).

increases with the voltage. For pores C and D (Figure 3b), both with annealed surfaces, the  $I$ – $V$  curves are symmetric and no rectification is observed (see Supporting Information for individual K<sup>+</sup> and Cl<sup>–</sup> ionic currents).

An estimate of the degree of ionic rectification is given by the rectification factor  $f_{\text{rec}}$ , defined as the absolute value of the ratio between the electric current measured for a given voltage with negative and positive signs. The closer  $f_{\text{rec}}$  is to 1, the less rectification arises. Table 2 shows the rectification factor  $f_{\text{rec}}$  at  $\pm 1$  V for six nanopores calculated using

$$f_{\text{rec}} = \frac{|I(-1 \text{ V})|}{|I(+1 \text{ V})|} \quad (8)$$

For 1 nm pores, pores A and B have considerable rectification, while pores C and D have less rectification (Table 2, second column).

Table 2 also shows the number of ions inside each nanopore under +1 and –1 V biases, averaged over the last 4 ns of each 10 ns trajectory. Nanopores that produce rectification (A, B, and E) accommodate different numbers of ions for each voltage polarity, the total number of ions being proportional to the ionic current. For crystalline pore A, the number of ions is higher at –1 V than at +1 V. A movie, PoreA, is provided in Supporting Information showing ion conduction through crystalline pore A under +1V and –1V biases; it shows that as the simulation progresses, the number of ions inside pore A becomes higher at –1V bias than at +1V bias. This pore also allows passage of more K<sup>+</sup> ions than Cl<sup>–</sup> ions. Conversely, for raw cut pores B and E the total number of ions is higher at +1 V than at –1 V. For raw cut pore B, the number of K<sup>+</sup> ions is close to the number of Cl<sup>–</sup> ions. In the case of pore E there are more K<sup>+</sup> ions than Cl<sup>–</sup> ions. Annealed pores C, D, and F show the same trend: there is no significant difference between the number of ions at +1 and –1 V, and the number of K<sup>+</sup> ions is close to the number of Cl<sup>–</sup> ions.

In the next sections, we will focus on 1 nm radius pores and investigate the dependence of ionic currents on the microscopic characteristic of nanopore surfaces.

**3.2. Ion Distribution inside Nanopores.** Previous MD studies with crystalline Si<sub>3</sub>N<sub>4</sub> nanopores<sup>12,13,62</sup> have shown that mainly K<sup>+</sup> ions adhere to the nanopore walls. The preference for K<sup>+</sup> over Cl<sup>–</sup> adsorption is due to the atomic-scale roughness of the crystalline Si<sub>3</sub>N<sub>4</sub> surface created by the removal of nitrogen and silicon atoms. Our results with SiO<sub>2</sub> pores reveal that the ion adsorption is due to surface topography and dangling atoms at the surface.

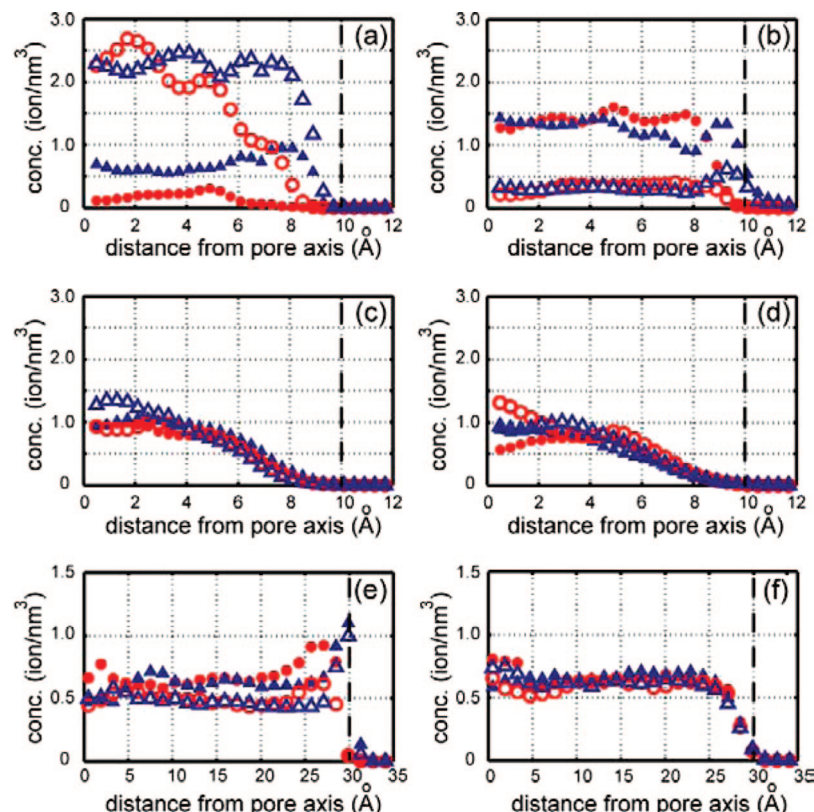


**Figure 4.** Ion concentrations as a function of radial distance from the nanopore axis. The figures show the ion concentration inside pores A (a), B (b), C (c), D (d), E (e), and F (f) using two voltage biases: +1 V (solid symbols) and -1 V (empty symbols). K<sup>+</sup> profiles are pictured as blue triangles and Cl<sup>-</sup> profiles as red circles. Dashed lines indicate the location of the nanopore wall.

All simulations involving nonannealed pores (A, B, C1, C2, and E) exhibited ion binding to the silica walls, similar to the ion binding observed in former studies of Si<sub>3</sub>N<sub>4</sub> pores.<sup>12,13,62</sup> However, simulations with annealed pores (C, D, and F) did not show any ion binding. A movie, C\_C1\_IV, is provided in Supporting Information showing ion conduction through annealed pore C and raw cut pore C1 at +1V bias; one can recognize that ions are only retained in a pore with dangling atoms at the surface, namely pore C1. The latter pores have a very low concentration of dangling atoms, revealing the roles of dangling atoms in ion adsorption.

Figure 4 shows the radial concentration of ions for six pores (see Methods). One can see that the concentration changes depending on pore surface and voltage polarity. The same concentration patterns are seen for all positive and negative voltage biases, only  $\pm 1$  V biases being presented. In the case of the crystalline and raw cut pores, a dramatic change of the concentration profile is observed for different voltage polarities. The crystalline pore A (Figure 4a) shows a significant increment in the ion concentration when changing from +1 to -1 V bias. The raw cut pore B shows the opposite (Figure 4b), the ion concentration being lower for a -1 V bias than for a +1 V bias. In contrast, annealed pores C and D show the same ion concentrations for +1 and -1 V biases (Figure 4, panels c and d). The radial ionic concentrations for 3 nm radius pores are presented in panels e and f of Figure 4. Pore E (Figure 4e) shows the same pattern as observed for pore B, a K<sup>+</sup> adsorption peak followed by a Cl<sup>-</sup> adsorption peak. The ion concentration in pore E is higher near the pore wall, converging to the bulk concentration at the center of the pore (1 M = 0.60 nm<sup>-3</sup>). The reason for the low rectification factor of pore E (see Table 2) is then that ions in the middle of the pore exhibit bulk properties. Pore F (Figure 4f) shows the same pattern observed

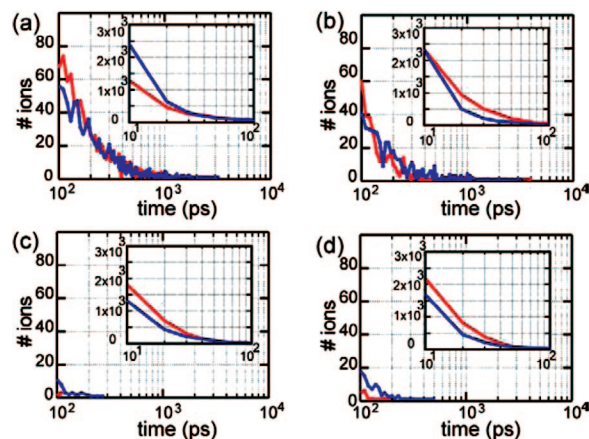


**Figure 5.** Residence times for 1 nm radius pores. The plots show the residence times for pores A (a), B (b), C (c), and D (d) under +1 V bias. The residence time of K<sup>+</sup> ions is shown in blue and that of Cl<sup>-</sup> ions in red. The ordinate axis shows the number of ions, and the abscissa axis shows the residence time from 100 to 10000 ps. The insets show numbers of ions with residence times from 10 to 100 ps.

for pores C and D, i.e., there are no ion adsorption peaks and the radial ionic concentrations for +1 V bias are equal to the ones observed for -1 V bias.

The adsorption of ions seen in our simulations is intermittent, depending on arrangement of dangling atoms at the surface and random collisions with other ions. Figure 5 shows the ion residence times for 1 nm radius pores and a +1 V bias (see Methods section); a similar pattern was obtained for a -1 V bias (see Supporting Information). The majority of ions have short residence times, ranging from 10 to 100 ps (see insets in Figure 5) and are not considered adsorbed, since such short residence times can be produced by random collisions. For pores



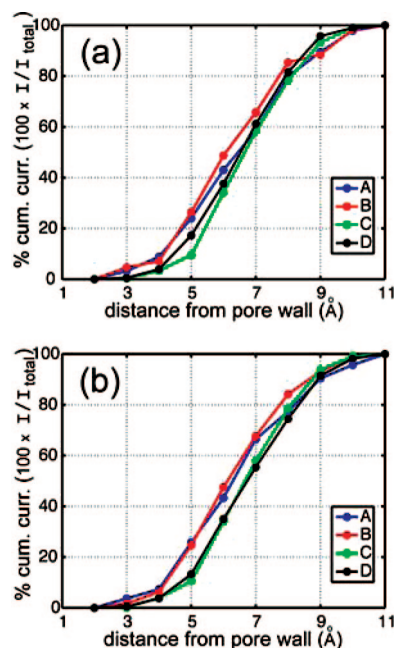


**Figure 6.** Ionic current near the nanopore wall for 1 nm radius pores. Figures show the percentage of the cumulative ionic current produced near the nanopore wall for pores A (blue), B (red), C (green), and D (black) under +1 V (a) and -1 V (b) biases. Plots were obtained by dividing the nanopore region in cylindrical rings. The outer surface of the ring is the nanopore wall while the inner surface is displaced from the wall toward the nanopore axis (abscissa axis). The ionic current for each cylindrical ring was computed using eq 2 and divided by  $I_{\text{total}}$ , the ionic current through the entire nanopore volume. Plots present the average values over the last 4 ns.

A and B (Figure 5, panels a and b, respectively), ions that move close to the silica surface are eventually adsorbed and released only with a significant delay, the residence times reaching up to several nanoseconds. Pores C and D do not adsorb ions on the surface, their residence times being therefore shorter.

By comparing the radial ion concentration and the residence times (Figure 4 and 5), it becomes clear that the surfaces of nonannealed pores (A and B) exhibit significant affinities for ions. The question arises, how much ions near the nonannealed surface contribute to the total current. The concentration of ions near the wall is high; therefore, the ionic current should be high in that region. However, since the residence time is long, the mobility is low, which implies a low current near the wall. Figure 6 shows the percentage of ionic current near the nanopore wall. If the ionic current is produced within 5 Å from the silica surface, it is considered in the “wall region”, otherwise it is considered in the “center region”. For nonannealed pores A and B, the ionic current near the wall is about 25% of the total current. For annealed pores C and D, the ionic current near the wall ranges from 10% to 17% of the total current. Even though pores A and B have higher ionic current near the wall, the majority of the current (about 75%) is still produced in the center of the pore.

**3.3. Ion–Silica Interactions.** To further investigate ion binding at nanopore walls, we performed four *single ion* simulations of voltage-driven translocations through two nanopores (see Methods), one with a high number of dangling atoms (pore B) and the other with a negligible number of dangling atoms (pore C). After the simulations were completed, we computed the potential energy using the plugin *NAMD Energy*<sup>65</sup> provided with VMD.<sup>53</sup> This calculation allowed us to disentangle the influence of ion–water and ion–silica interactions while not accounting for ion–ion interactions.

The experimental values for the hydration free energies of  $\text{K}^+$  and  $\text{Cl}^-$  ions have been estimated to be around -80 and -85 kcal/mol.<sup>77,78</sup> The values obtained with *NAMD Energy* exceed experimental values for several reasons: (i) *NAMD Energy* only calculates the potential energy component ( $U$ ), which is computed between two selections of atoms, ignoring the rest of the system; (ii) there exist inaccuracies in the silica force field as well as in the water and ion force fields; (iii) details in the simulation protocol (cutoff distance, periodic conditions) also affect calculated energy values. Even though the computed energies are affected to a great extent by the stated shortcomings, they provide nevertheless a valuable qualitative description of the energetic variations actually experienced by ions.

The ion movements across the nanopore and the associated ion–water and ion–silica energies are presented in Figure 7. Figure 7b shows the translocation of a  $\text{K}^+$  ion through pore B. Initially, the  $\text{K}^+$  ion moved randomly for 5.7 ns in the cis compartment. In that region, the ion–water interaction energy was dominant (Figure 7a), while the ion–silica interaction energy was zero (region i). From 5.7 to 7 ns, the ion reached and touched the upper surface without yet entering into the pore, producing a negative increase of the ion–silica energy (region ii). When the surface was touched, a partial removal of the ion’s solvation shell produced a decrease in the absolute value of the ion–water energy and an increase in the ion–silica energy. After the initial surface contact, the  $\text{K}^+$  moved back into the cis solvent compartment (region iii), the negative increment in the ion–water energy indicating that the water shell was restored. Then at 9.5 ns the ion moved again near the nanopore opening. The sharp spikes observed in the energy profiles (region iv, Figure 7a) were due to an initial ion binding to the surface. The ion was released from the surface at 10 ns and quickly moved through the nanopore (region v, Figure 7b) until it was absorbed again by the surface at 10.8 ns, 10 Å away from the pore exit. The snapshot on the right-hand side shows the  $\text{K}^+$  ion in direct contact with two dangling oxygens (pictured in purple), its water shell partially removed. Subsequently, the ion bounced between solvent and surface (region vi), as is evident through the oscillations in the ion–water and ion–silica energies.

Figure 7d shows the translocation of a  $\text{K}^+$  ion through pore C. The single  $\text{K}^+$  ion reached the nanopore opening at 3.3 ns, moved through the nanopore, and was finally released into the trans compartment at 4.9 ns. The snapshot on the right-hand side shows the  $\text{K}^+$  ion in the middle of the pore. During the entire translocation, the  $\text{K}^+$  ion kept its solvation shell, the ion–water potential energy remained constant, while the ion–silica potential energy was negligible. Similar scenarios were observed for conduction of a single  $\text{Cl}^-$  ion through pores B and C (see Supporting Information).

The presented results provide a complete picture of ion translocation and surface binding processes. To capture an ion, the surface has to provide a location that can compensate the energetic cost of removing the ion’s water shell.<sup>66</sup> Due to their accessibility, dangling atoms have high affinities for ions; however, they need to arise in a group of two or more to effectively produce ion binding. Since the gaps on the raw cut and crystalline surfaces were previously filled with silicon and oxygen atoms, i.e., are wide enough to permit access to ions, the patches of dangling atoms are geometrically optimized for retaining ions. When a uniform electric field is applied, ions move through the pore. When an ion moves near a patch of dangling atoms, it is adsorbed. The adsorption is intermittent and affects the ion concentration profile inside the pore. A movie, *Kbind*, is provided in Supporting Information illustrating

the adsorption of a  $K^+$  ion in an area covered by two dangling oxygens, the ion's water shell being partially removed upon binding. On the other hand, surfaces of annealed pores are not able to dehydrate ions. After annealing, the silica surface rearranges and the patches of dangling atoms are removed. The interaction energy between an ion and an annealed surface cannot compensate for the energetic penalty of removing the hydration shell, and ions are not adsorbed.

**3.4. The Electrostatic Potential.** Under a uniform electric field, the simulated system responds by rearranging all mobile charged species. Water molecules and ions move around the simulation cell trying to counterbalance the applied electrostatic potential.<sup>12</sup> As a result, the mean electrostatic potential  $V_{\text{mean}}^e(Z)$  (see eq 3) is nonuniform and has two contributions, one from the applied uniform potential and the other from the reaction potential, produced by the location of all charges. Since the ion distribution inside the nanopore depends on the characteristics of the pore surface,  $V_{\text{mean}}^e(Z)$  is expected to differ among the various pores. The contour plots in Figure 8 display  $V_{\text{mean}}^e(Z)$  for 1 nm radius pores under voltage biases  $\varepsilon$  of +1 and -1 V. In the case of annealed pores C and D,  $V_{\text{mean}}^e(Z)$  for +1 V (Figure 8e,g) is approximately the inverted image of the potential obtained for -1 V (Figure 8f,h). In the case of pores A and B, bias inversion produces mean electrostatic potentials that, if turned upside down, do not overlap.

To investigate how the electrostatic potential affects the ionic current, we computed the electrostatic force  $F^e(Z)$  acting on a probe of charge  $e$ ,  $F^e(Z)$  including all electrostatic contributions, i.e., external and intrinsic potentials.  $F^e(Z)$  was calculated using

$$F^e(Z) = -Q\partial_Z V_{\text{fit}}^e(Z) \quad (9)$$

where  $V_{\text{fit}}^e(Z)$  is the mean electrostatic potential along the pore axis at  $\varepsilon$  bias (see Methods, eq 6),  $Q$  is an elementary charge, namely,  $e$  ( $+1.6 \times 10^{-19}$  C), and  $\partial_Z$  denotes the derivative with respect to  $Z$ . At +1 V bias, the sign of the electrostatic force is positive and the probe charge moves from the trans to the cis compartment. At -1 V bias the force acting is negative, and the probe moves in the opposite direction. In Figure 9 we present  $F^e(Z)$  for 1 nm radius pores at  $\pm 1$  V biases, i.e.,  $F^{+1V}(Z)$  and  $F^{-1V}(Z)$ . As expected,  $F^e(Z)$  is strongest in the pore region. Moreover, crystalline and raw cut pores produce asymmetric responses when inverting the polarity. In crystalline pore A (Figure 9a),  $F^{+1V}(Z)$  is higher in the absolute value than  $F^{-1V}(Z)$ . The opposite is observed for raw cut pore B (Figure 9b) where  $F^{+1V}(Z)$  is lower in the absolute value than  $F^{-1V}(Z)$ . The asymmetry in the force profile is only observed in pores that produce rectification, while in the case of annealed pores C and D (Figure 9c,d) the force profiles are symmetric and  $F^{+1V}(Z)$  is approximately the inverted image of  $F^{-1V}(Z)$ , i.e.,  $F^{+1V}(Z) \approx F^{-1V}(Z)$ .

Lastly, we computed the potential  $V_{\text{syst}}(Z)$  defined in eq 7 that reflect the intrinsic pore electrostatics without the influence of the applied bias. As shown in Figure 10,  $V_{\text{syst}}(Z)$  exhibits an asymmetric  $Z$  dependence for nonannealed pores A and B (Figure 7a,b). It had been proposed that electrostatic potentials of such asymmetric “saw-tooth” shape produce rectification,<sup>35</sup> where the height of the electrostatic barrier is shifted depending on the polarity of the applied voltage. The different shifts increase the ion conduction in one direction and decrease it in

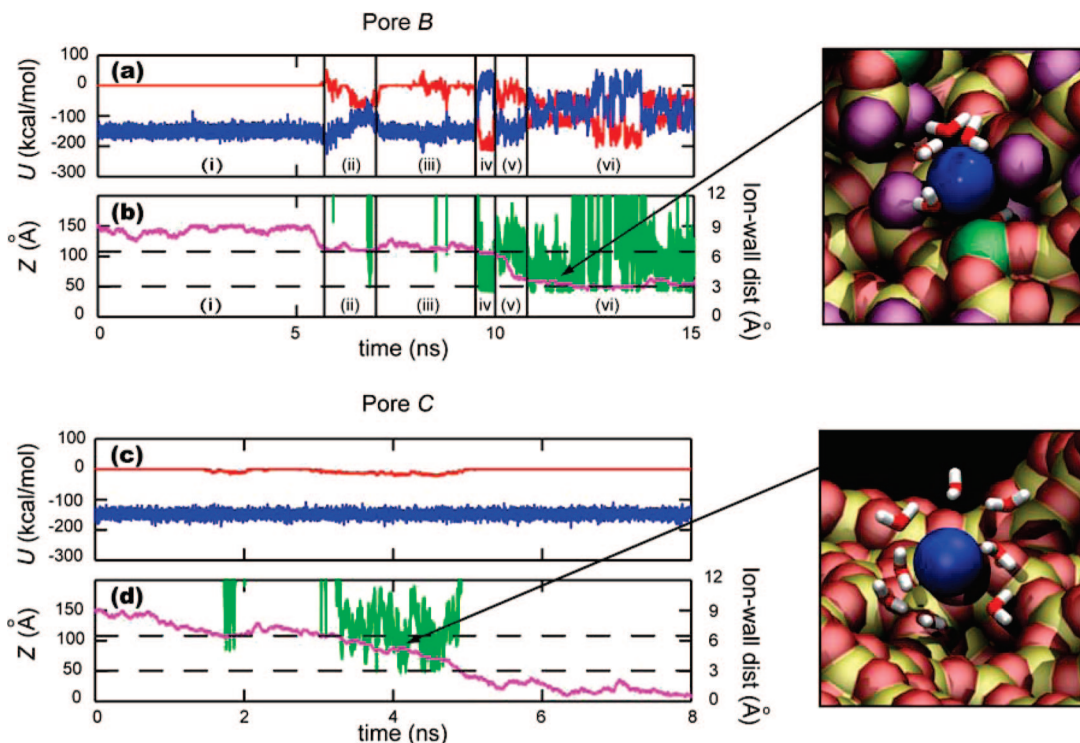


**Figure 7.** Voltage-driven translocation of a single  $K^+$  ion through silica nanopores. The plots on the left-hand side show the potential energy (a, c) and location (b, d) of a single  $K^+$  ion voltage driven through raw cut pore B (a, b) and annealed pore C (c, d). Magenta lines show the ion location along the  $Z$  axis (scale on the left ordinate axis), green lines show the radial distance between the ion and the nanopore wall (scale on the right ordinate axis) as a function of time (abscissa axis). The horizontal black dashed lines are reference lines to indicate the boundaries of the silica pores. For a complete ion translocation from the cis to the trans compartment, the magenta line has to cross both black lines. The blue and red lines show the associated ion–water and ion–silica potential energies, respectively. The snapshots on the right-hand side show the  $K^+$  ion at a specific moment during translocation.  $K^+$  is pictured in blue. Silica atoms are colored as follows: nondangling silicon in yellow, nondangling oxygen in red, dangling silicon in green and dangling oxygens in purple. Water molecules are shown in licorice representation (oxygen red, hydrogen white). Atomic events in regions (i–vi) are described in the text.



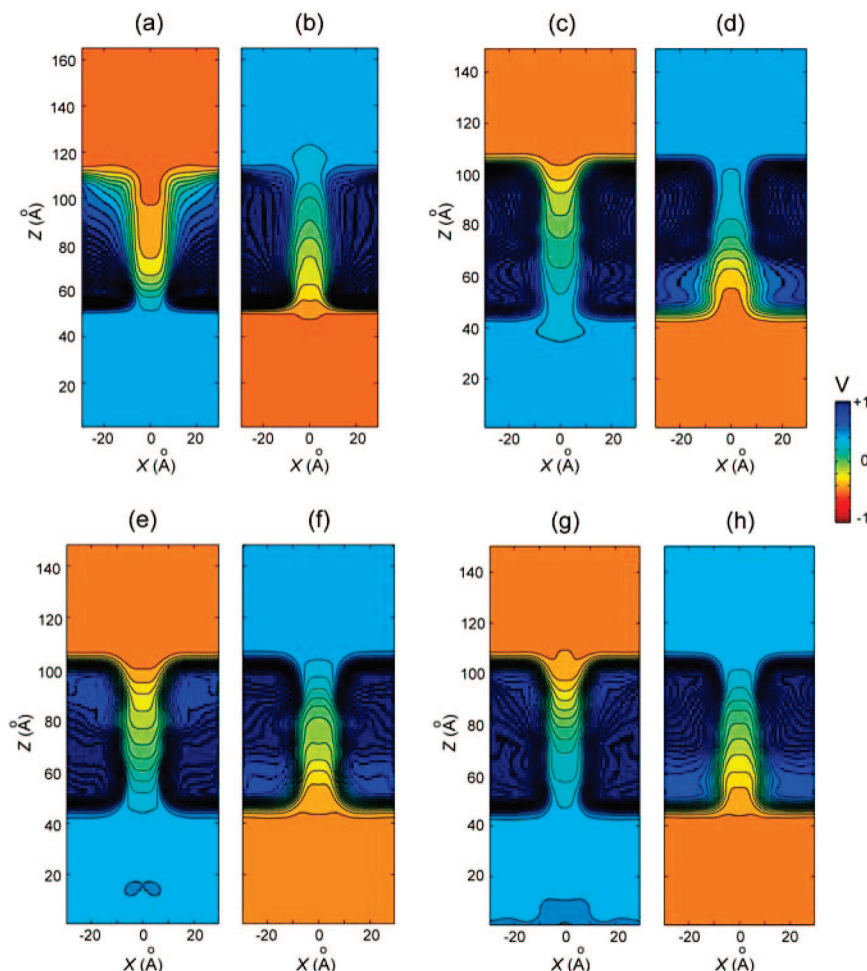


**Figure 8.** Mean electrostatic potentials  $V_{\text{mean}}^e(\mathbf{r})$ . Contour plots show the mean electrostatic potential of 1 nm radius pores for two voltage biases. Pore A was studied under +1 V (a) and -1 V (b), pore B under +1 V (c) and -1 V (d), pore C under +1 V (e) and -1 V (f), and pore D under +1 V (g) and -1 V (h).  $V_{\text{mean}}^e(\mathbf{r})$  was computed using eq 3. One can recognize that  $V_{\text{mean}}^e(r)$  depends on the silica surface.

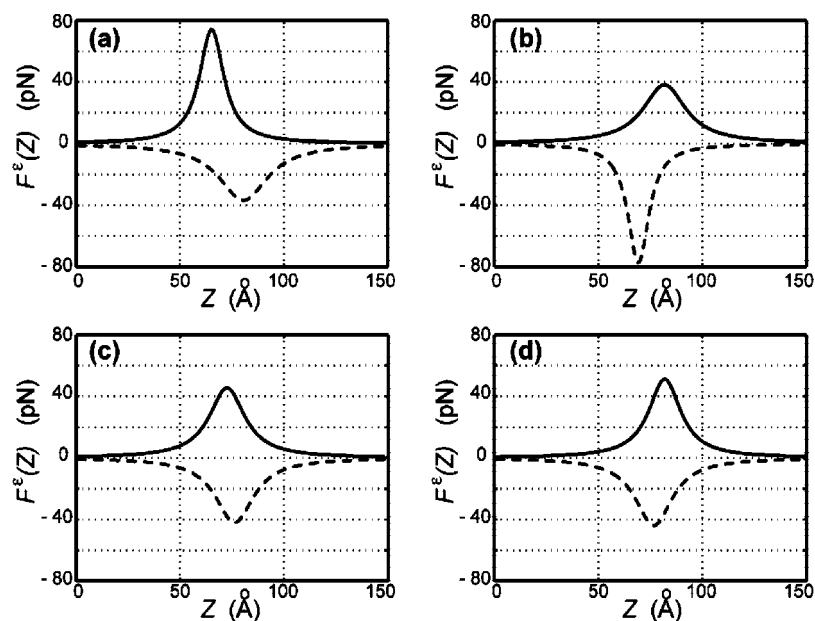


**Figure 9.** Electrostatic force  $F^e(Z)$  inside 1 nm radius pores. Plots show the electrostatic force acting on a probe charge of  $e$  for pores A (a), B (b), C (c), and D (d). Solid lines show  $F^{+1V}(Z)$ , the electrostatic force under +1 V bias. Dashed lines show  $F^{-1V}(Z)$ , the electrostatic force under -1 V bias. Trans, nanopore, and cis regions are located in the intervals [0–50 Å], [50–100 Å], and [100–150 Å] along the  $Z$  axis, respectively.

the opposite direction, producing rectification. For annealed pores C and D,  $V_{\text{sys}}(Z)$  exhibits low values and a symmetric  $Z$  dependence (Figure 10c,d).

**3.5. Atomic Origin of Ionic Rectification.** In the previous section, we showed that ionic rectification is related to an asymmetric electrostatic potential. In the following, we seek to

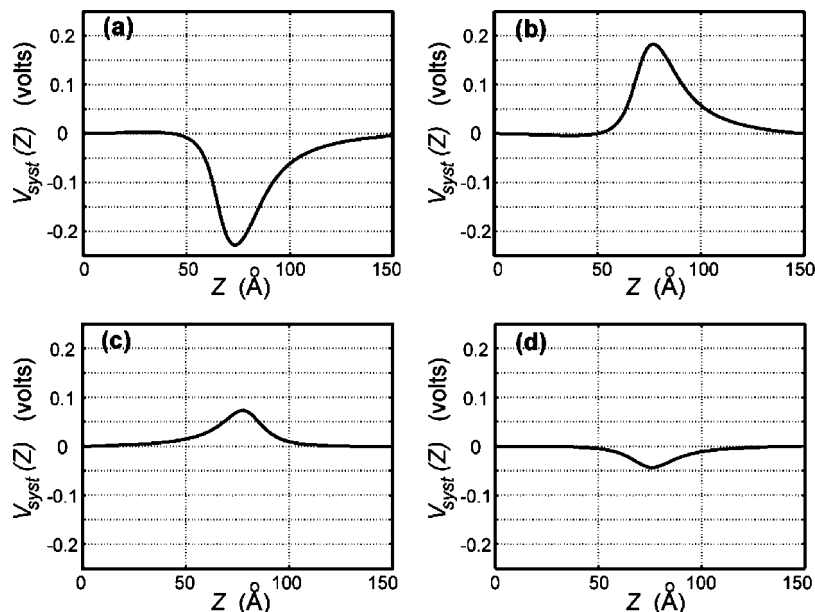


**Figure 10.** Electrostatic potential  $V_{\text{syst}}(Z)$  for 1 nm radius pores. Plots show  $V_{\text{syst}}(Z)$  for pores A (a), B (b), C (c), and D (d). The systems are composed of silica nanopores and 1 M KCl solution.  $V_{\text{syst}}(Z)$  was computed using eq 7. Trans, nanopore, and cis regions are located in the intervals [0–50 Å], [50–100 Å], and [100–150 Å] along the  $Z$  axis, respectively.

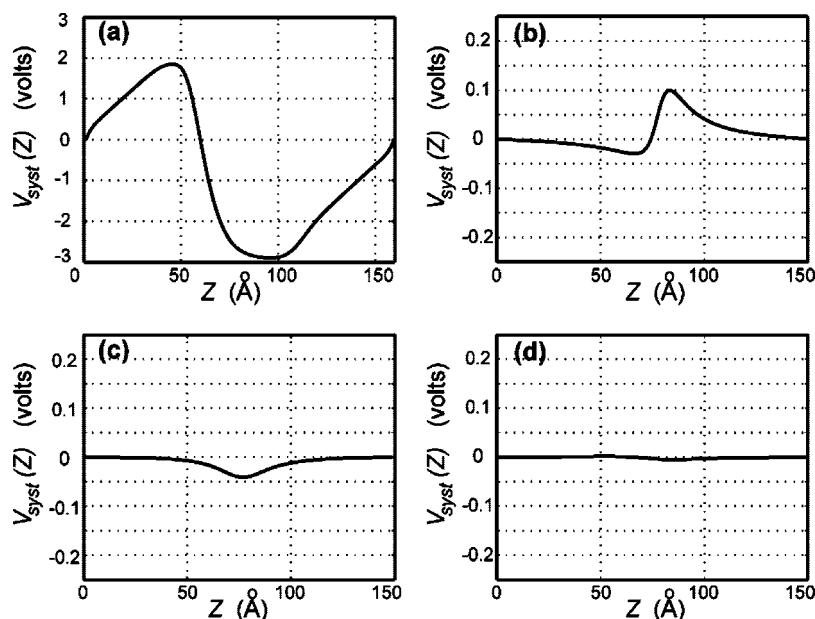


**Figure 11.** Electrostatic potential  $V_{\text{syst}}(Z)$  for 1 nm radius pores. Plots show  $V_{\text{syst}}(Z)$  for pores A (a), B (b), C (c), and D (d). The systems are composed of silica nanopores and water without ions.  $V_{\text{syst}}(Z)$  was computed using eq 7. Trans, nanopore, and cis regions are located in the intervals [0–50 Å], [50–100 Å], and [100–150 Å] along the  $Z$  axis, respectively. Note that plot (a) has a different scale for  $V_{\text{syst}}(Z)$ .

explain the origin of this asymmetry in atomic detail. Specifically, we ask how an asymmetric electrostatic potential arises in a system with a seeming front–back symmetry and why the rectification observed in pores A and B enhances ionic current in opposite directions.

In our MD systems, there are only two charged species that can be responsible for the asymmetry, the silica surface structure and the adsorbed ions. To investigate the electrostatic contribution arising from the silica structure, we simulated the 1 nm radius pores under  $\pm 1$  V biases, but with all KCl removed (see Table 1). Figure 11 shows the electrostatic potential  $V_{\text{syst}}(Z)$ , which now refers to systems composed of silica nanopores without any ions. Pores with a high number of dangling atoms at the surface (i.e., pores A and B) have an asymmetric  $V_{\text{syst}}(Z)$ . Pore A constitutes the most dramatic case, where the asymmetry

actually extends beyond the nanopore region and includes also the cis and trans regions (Figure 11a). The reason is that pore A was obtained from a cristobalite silica cube: on the cis side of the solvent compartment, crystalline silica exposes the (001) face covered with negatively charged dangling oxygens, while on the trans side of the solvent compartment, crystalline silica exposes its (00 $\bar{1}$ ) face covered with positively charged dangling silicons. Figure 12 shows the number of dangling oxygen and silicon atoms along the  $Z$  axis. The nonhomogeneous distribution of dangling atoms observed in pore A (Figure 12a) is a result of the crystalline arrangement and magnifies the effects of dangling atoms. For pore B, the asymmetry of  $V_{\text{syst}}(Z)$  arises only in the nanopore region (Figure 11b); the distribution of dangling atoms is fuzzy and does not show any particular pattern (Figure 12b). For pores with a negligible number of dangling

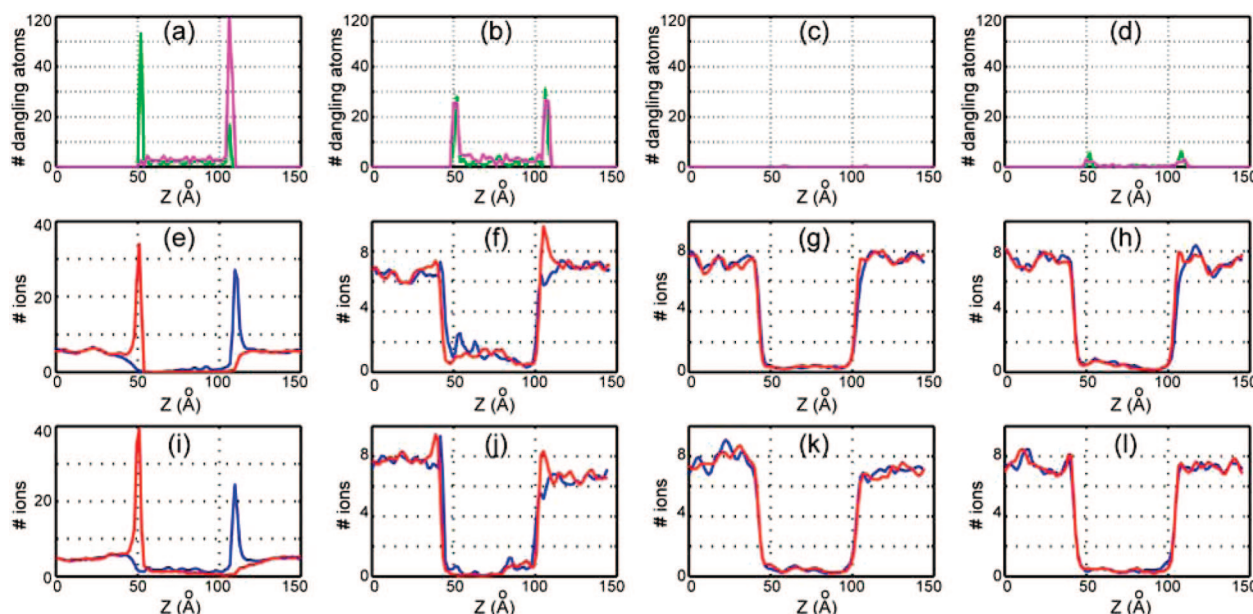


**Figure 12.** Dangling atoms and ion distribution for 1 nm radius pores. The first row shows the number of dangling oxygens (purple lines) and dangling silicons (green lines) for pores A (a), B (b), C (c), and D (d) along the Z axis. The second and third rows show the number of  $K^+$  (blue lines) and  $Cl^-$  (red lines) ions along the Z axis for systems with pores A (e, i), B (f, j), C (g, k), and D (h, l) under +1 V (e–h) and –1 V (i–l) biases. Trans, nanopore, and cis regions are located in the intervals [0–50 Å], [50–100 Å], and [100–150 Å] along the Z axis, respectively.

atoms such as pores C (Figure 12c) and D (Figure 12d),  $V_{\text{sys}}(Z)$  is symmetric and assumes only small values (Figure 11c,d). A comparison of  $V_{\text{sys}}(Z)$  with and without ions (Figures 10 and 11) demonstrates that the presence of dangling atoms is the main source for the electrostatic asymmetry; the adsorbed ions have also an effect on the asymmetry, altering  $V_{\text{sys}}(Z)$  and focusing the voltage drop inside the pore.

The direction of the ionic rectification in pore A can be explained through the dangling atom distribution and the resulting adsorbed ions. Figure 12e–l shows the number of ions along the Z axis averaged over the last 4 ns of simulations with 1 M KCl under  $\pm 1$  V biases. In the case of pore A (Figure 12e,i), the ion distribution is a response to the ordered structure of the dangling atoms, with two distinctive  $K^+$  and  $Cl^-$  adsorption peaks near the (001) and (00  $\bar{1}$ ) silica faces, respectively. The increment in the number of  $K^+$  ions near the cis pore opening and  $Cl^-$  ions near the trans pore opening enhances ionic current at negative biases, where  $K^+$  ions translocate from cis to trans and  $Cl^-$  ions from trans to cis. A movie, PoreA, is provided in Supporting Information showing recruitment of  $K^+$  ions near the cis pore opening; the ions move eventually into the pore at –1 V bias. The reason for the direction of the rectification in pore B is not clear. The ion distribution (Figure 12f,j) shows that there are several ion adsorption peaks at the pore openings and in the nanopore region; however, it is difficult to establish a relationship among the number of dangling atoms (Figure 12b), the ion distribution (Figure 12f,j), and the direction of ionic rectification (Figure 3a). In pore B, the structure is amorphous and the number of dangling atoms and the respective ion adsorption patterns do not have the simple organization as seen for pore A.

Another set of simulations was performed to investigate why the amorphous raw cut surface of pore B produces an ion current rectification opposite to the one observed in pore A. We used annealed pore C as a template to produce two nanopores that expose an amorphous raw cut surface only in the nanopore region. The first pore, called C1, was built by removing atoms located within a 1.3 nm distance from the Z axis of pore C.

The second pore, called C2, was built by removing 7 dangling silicons and 14 dangling oxygens from the amorphous surface of pore C1; the deletion of the dangling oxygens creates new dangling silicons, and vice versa. Consequently, both pores C1 and C2 expose amorphous raw cut surfaces at the nanopore region and have 1.3 nm radius pores, but differ only in the distribution of the dangling atoms. Figure 13 shows the nanopores and the number of dangling atoms along the Z axis. The nanopores were solvated, ionized with 1 M KCl, and simulated under  $\pm 1$  V biases (see Table 1). The simulations were performed for 30 ns to provide a wider sample for the computed average currents. Table 3 presents the ionic currents and the rectification factor,  $f_{\text{rec}}$ . The rectification effect for pore C1 is similar to that for pore A, enhancing the ionic current in the case of a negative voltage. In the case of pore C2, the rectification is inverted relative to that for pore C1, producing a rectification effect similar that for pore B. The different rectification factors  $f_{\text{rec}}$  confirm that the distribution of dangling atoms determines the direction of the ionic rectification for raw cut amorphous pores. Pore B was obtained by cutting the surface of an amorphous cube, and the particular location of dangling atoms was determined by chance. A different cut would expose a different surface and would have a different effect on the ionic current and rectification.

Our results are consistent with previous studies. Several models for rectification have been proposed<sup>28,36,37</sup> based on interactions between ions translocating a negatively charged pore, the pore being narrow enough to allow ion–surface interactions (for a detailed review, see ref 35 and references therein). In all cases, the ion current rectification arises when the symmetry of the electrostatic potential is broken. The scenario we presented here is like those described in refs 28, 36, and 37, but instead of breaking the electrostatic symmetry through conical geometry or surface charges, our pores exhibit an asymmetric distribution of dangling atoms with different affinities for cations and anions. Furthermore, our results provide new insights into the rectification phenomenon. In nanopores with rectification, we observed desolvation and temporal adsorp-



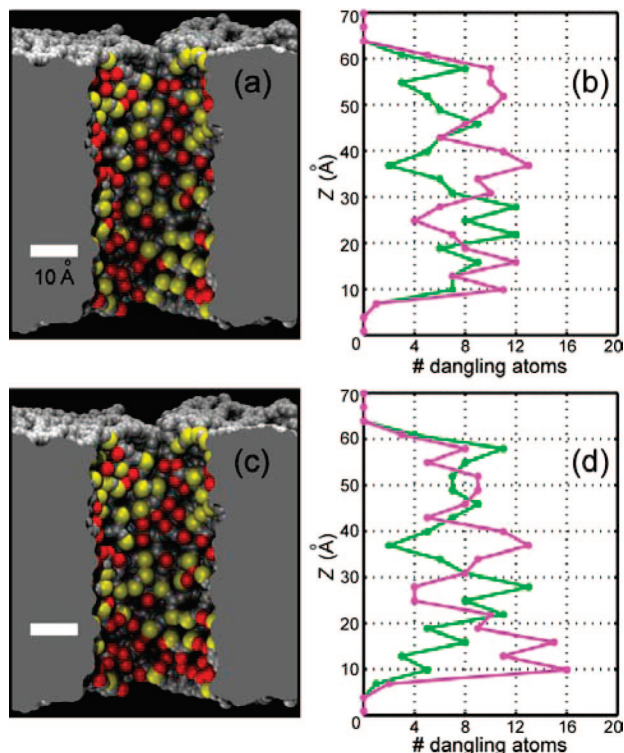


**Figure 13.** Atomic models of nanopores C1 and C2. Figures at left show two nanopores, namely, pores C1 (a) and C2 (c). Both pores present a raw cut surface in contact with the nanopore region and annealed surface in contact with the cis and trans compartments. Dangling silicons are shown in yellow, dangling oxygens in red, and nondangling oxygens and nondangling silicons in gray. Plots at right show the number of dangling silicon (green lines) and dangling oxygen (purple lines) atoms along the Z axis for pores C1 (b) and C2 (d).

**TABLE 3: Rectification factor,  $f_{\text{rec}}$ , for pores C1 and C2<sup>a</sup>**

nanopore	$I(+1 \text{ V})$ (nA)	$I(-1 \text{ V})$ (nA)	$f_{\text{rec}}$
C1	2.24	-3.04	$1.36 \pm 0.06$
C2	3.34	-2.49	$0.75 \pm 0.03$

<sup>a</sup> Nanopores are listed in the first column. Ionic currents under +1 and -1 V bias are shown in the second and third columns, respectively.  $f_{\text{rec}} \pm$  its standard error are shown in the fourth column. The average ionic currents were calculated over the last 20 ns of each 30 ns MD simulation.

tion of ions which redistribute the voltage drop inside the pore. Moreover, rectification was associated with different total ionic concentration at opposite voltage biases (Table 2). Ion selectivity can be observed (pore A) but was not necessary for rectification (pore B). Finally, the atomic detail provided by MD simulations allowed us to perform thorough analyses, such as inspecting the radial ionic concentration inside the pore, residence times for ions, amount of current near the wall, and electrostatic contributions of every component of the system.

#### 4. Conclusions

Through MD simulations we have performed a systematic study of ion current rectification observed in nanopores. For this purpose, we built eight silica nanopore models, four of 1 nm radius, two of 1.3 nm radius, and two of 3 nm radius, and simulated them immersed in KCl and for a variety of voltage biases. Our simulations showed that ion current rectification is due to an asymmetric distribution of ion-binding spots on the silica surface. We offer an atomic-level description of the rectification phenomenon. Nanopores that produce ion current

rectification expose ion-binding spots, namely, dangling atoms. These spots have the ability to dehydrate ions and temporally bind them to the surface, affecting the ion distribution inside the pore. An asymmetric distribution of dangling atoms generates then an asymmetric electrostatic potential, and when the polarity is inverted, it produces different electrostatic profiles and consequently current rectification. Conversely, nanopores that lack dangling atoms are unable to dehydrate and retain ions, exhibit symmetric electrostatic potentials, and produce symmetric ohmic responses.

We previously proposed an explanation of the initial hydrophobicity of manufactured silica nanopores<sup>48</sup> and now provide an atomistic description of ion current often observed in nanopores. Our results validate the use of MD simulations as valuable tools for studying nanoscale systems, where the atomic details of the solvent and the solid surface play a major role. MD models could also be used to study other ion current phenomena observed in nanopores, such as current hysteresis or current fluctuations due to  $\text{Ca}^{2+}$  ions as well as the interactions between biological macromolecules and silica surfaces.

**Acknowledgment.** We thank David Hardy for modifying NAMD-lite to perform silica annealing cycles. We also thank the members of the Theoretical and Computational Biophysics Group for helpful discussions. This work is supported by grants from NIH (P41-RR05969, R01-HG003713), NSF (CCR-02-1084, PHY0822613), and the Petroleum Research Fund (48352-G6). We acknowledge supercomputer time provided at the National Center for Supercomputing Applications through National Resources Allocation Committee Grant (MCA93S028, MCA05S028) and at the Turing Xserve Cluster funded by the University of Illinois at Urbana-Champaign.

**Supporting Information Available:** Figures showing  $I-V$  curves for individual  $\text{K}^+$  and  $\text{Cl}^-$  ionic currents, residence times at -1 V bias, and analysis for the voltage-driven translocation of a single  $\text{Cl}^-$  ion and three movies showing ion rectification in pore A (PoreA), ion conductions through annealed and nonannealed pores (C\_C1\_1V), and  $\text{K}^+$  ion adsorption (Kbind). This material is available free of charge via the Internet at <http://pubs.acs.org>.

#### References and Notes

- (1) Kam, N. W. S.; O'Connell, M.; Wisdom, J. A.; Dai, H. *Proc. Natl. Acad. Sci. U.S.A.* **2005**, *102*, 11600–11605.
- (2) Patolsky, F.; Zheng, G.; Lieber, C. M. *Anal. Chem.* **2006**, *78*, 4260–4269.
- (3) Dekker, C. *Nat. Nanotechnol.* **2007**, *2*, 209–215.
- (4) Feynman, R. P. *Eng. Sci.* **1960**, *23*, 22–36.
- (5) Lu, D.; Aksimentiev, A.; Shih, A. Y.; Cruz-Chu, E.; Freddolino, P. L.; Arkhipov, A.; Schulten, K. *Phys. Biol.* **2006**, *3*, S40–S53.
- (6) Aksimentiev, A.; Brunner, R.; Cohen, J.; Comer, J.; Cruz-Chu, E.; Hardy, D.; Rajan, A.; Shih, A.; Sigalov, G.; Yin, Y.; Schulten, K. In *Protocols in Nanostructure Design, Methods in Molecular Biology*; Humana Press: Totowa, NJ, 2008; pp 181–234.
- (7) Service, R. F. *Science* **2006**, *311*, 1544–1546.
- (8) Sigalov, G.; Comer, J.; Timp, G.; Aksimentiev, A. *Nano Lett.* **2008**, *8*, 56–63.
- (9) Storm, A. J.; Chen, J. H.; Ling, X. S.; Zandbergen, H. W.; Dekker, C. *Nat. Mater.* **2003**, *2*, 537–540.
- (10) Ho, C.; Qiao, R.; Heng, J. B.; Chatterjee, A.; Timp, R. J.; Aluru, N. R.; Timp, G. *Proc. Natl. Acad. Sci. U.S.A.* **2005**, *102*, 10445–10450.
- (11) Siwy, Z.; Apel, P.; Baur, D.; Dobrev, D. D.; Korchev, Y. E.; Neumann, R.; Spohr, R.; Trautmann, C.; Voss, K. *Surf. Sci.* **2003**, *532*, 1061–1066.
- (12) Aksimentiev, A.; Heng, J. B.; Timp, G.; Schulten, K. *Biophys. J.* **2004**, *87*, 2086–2097.
- (13) Heng, J. B.; Ho, C.; Kim, T.; Timp, R.; Aksimentiev, A.; Grinkova, Y. V.; Sligar, S.; Schulten, K.; Timp, G. *Biophys. J.* **2004**, *87*, 2905–2911.

- (14) Zhao, Q.; Comer, J.; Yemenicioglu, S.; Aksimentiev, A.; Timp, G. *Nucleic Acids Res.* **2008**, *36*, 1532–1541.
- (15) Zhao, Q.; Sigalov, G.; Dimitrov, V.; Dorvel, B.; Mirsaidov, U.; Sliger, S.; Aksimentiev, A.; Timp, G. *Nano Lett.* **2007**, *7*, 1680–1685.
- (16) Comer, J.; Dimitrov, V.; Zhao, Q.; Timp, G.; Aksimentiev, A.; *Biophys. J.* **2009**, *96*, 593–608.
- (17) Muckhopadhyay, R. *Anal. Chem.* **2006**, *78*, 7379–7382.
- (18) Stein, D.; Kruithof, M.; Dekker, C. *Phys. Rev. Lett.* **2004**, *93*, 035901-1–035901-4.
- (19) Luan, B.; Aksimentiev, A. *Phys. Rev. E* **2008**, *78*, 021912-1–021912-4.
- (20) van der Heyden, F. H. J.; Stein, D.; Dekker, C. *Phys. Rev. Lett.* **2005**, *95*, 116104-1–116104-4.
- (21) Smeets, R. M. M.; Keyser, U. F.; Krapf, D.; Wu, M. Y.; Dekker, N. H.; Dekker, C. *Nano Lett.* **2006**, *6*, 89–95.
- (22) Smeets, R. M. M.; Keyser, U. F.; Wu, M. Y.; Dekker, N. H.; Dekker, C. *Phys. Rev. Lett.* **2006**, *97*, 088101-1–088101-4.
- (23) van der Heyden, F. H. J.; Stein, D.; Besteman, K.; Lemay, S. G.; Dekker, C. *Phys. Rev. Lett.* **2006**, *96*, 224502-1–224502-4.
- (24) Lorenz, C. D.; Travesset, A. *Phys. Rev. E* **2007**, *75*, 061202-1–061202-5.
- (25) Siwy, Z. S.; Powell, M. R.; Petrov, A.; Kalman, E.; Trautmann, C.; Eisenberg, R. S. *Nano Lett.* **2006**, *6*, 1729–1734.
- (26) Siwy, Z. S.; Powell, M. R.; Kalman, E.; Astumian, R. D.; Eisenberg, R. S. *Nano Lett.* **2006**, *6*, 473–477.
- (27) Siwy, Z.; Gu, Y.; Spohr, H. A.; Baur, D.; Wolf-Reber, A.; Spohr, R.; Apel, P.; Korchev, Y. E. *Europhys. Lett.* **2002**, *60*, 349–355.
- (28) Cervera, J.; Schiedt, B.; Neumann, R.; Mafé, S.; Ramírez, P. *J. Chem. Phys.* **2006**, *124*, 104706-1–104706-9.
- (29) Powell, M. R.; Sullivan, M.; Vlassioun, I.; Constantin, D.; Sudre, O.; Martens, C. C.; Eisenberg, R. S.; Siwy, Z. S. *Nat. Nanotechnol.* **2008**, *3*, 51–57.
- (30) Daiguji, H.; Oka, Y.; Shirono, K. *Nano Lett.* **2005**, *5*, 2274–2280.
- (31) Vlassioun, I.; Siwy, Z. S. *Nano Lett.* **2007**, *7*, 552–556.
- (32) Karnik, R.; Duan, C.; Castellino, K.; Daiguji, H.; Majumdar, A. *Nano Lett.* **2007**, *7*, 547–551.
- (33) Gijs, M. A. M. *Nat. Nanotechnol.* **2007**, *2*, 268–270.
- (34) Siwy, Z.; Kosińska, I. D.; Fuliński, A.; Martin, C. R. *Phys. Rev. Lett.* **2005**, *94*, 048102-1–048102-4.
- (35) Siwy, Z. S. *Adv. Funct. Mater.* **2006**, *16*, 735–746.
- (36) Constantin, D.; Siwy, Z. *Phys. Rev. E* **2007**, *76*, 041202-1–041202-10.
- (37) Wang, X.; Xue, J.; Wang, L.; Guo, W.; Zhang, W.; Wang, Y.; Liu, Q.; Ji, H.; Ouyang, Q. *J. Phys. D: Appl. Phys.* **2007**, *40*, 7077–7084.
- (38) Schuss, Z.; Nadler, B.; Eisenberg, R. S. *Phys. Rev. E* **2001**, *64*, 036116-1–036116-14.
- (39) Krapf, D.; Quinn, B. M.; Wu, M.-Y.; Zandbergen, H. W.; Dekker, C.; Lemay, S. G. *Nano Lett.* **2006**, *6*, 2531–2535.
- (40) Kim, D.; Darve, E. *Phys. Rev. E* **2006**, *73*, 051203-1–051203-12.
- (41) Qiao, R. *Microfluid. Nanofluid.* **2007**, *3*, 33–38.
- (42) Gallo, P.; Rapinesi, M.; Rovere, M. *J. Chem. Phys.* **2002**, *117*, 369–375.
- (43) Shirono, K.; Daiguji, H. *J. Phys. Chem. C* **2007**, *111*, 7938–7946.
- (44) Leung, K.; Rempe, S. B.; Lorenz, C. D. *Phys. Rev. Lett.* **2006**, *96*, 095504-1–095504-4.
- (45) Joseph, S.; Aluru, N. R. *Langmuir* **2006**, *22*, 9041–9051.
- (46) Braun, R.; Sarikaya, M.; Schulten, K. *J. Biomat. Sci.* **2002**, *13*, 747–758.
- (47) Ghiringhelli, L. M.; Hess, B.; van der Vegt, N. F. A.; Delle Site, L. *J. Am. Chem. Soc.* **2008**, *130*, 13460–13464.
- (48) Cruz-Chu, E. R.; Aksimentiev, A.; Schulten, K. *J. Phys. Chem. B* **2006**, *110*, 21497–21508.
- (49) *Cerius<sup>2</sup>, v.4.9*; Accelrys, Inc., 9685 Scranton Rd, San Diego, CA 92121, 2003.
- (50) NAMD-Lite is a collection of C libraries to enable the development of methods for molecular dynamics. URL: <http://www.ks.uiuc.edu/Development/MDTools/mdx/>.
- (51) Phillips, J. C.; Braun, R.; Wang, W.; Gumbart, J.; Tajkhorshid, E.; Villa, E.; Chipot, C.; Skeel, R. D.; Kale, L.; Schulten, K. *J. Comput. Chem.* **2005**, *26*, 1781–1802.
- (52) *Matlab v.6*, The MathWorks, Natick, MA, 2002.
- (53) Humphrey, W.; Dalke, A.; Schulten, K. *J. Mol. Graphics* **1996**, *14*, 33–38.
- (54) van Beest, B. W. H.; Kramer, G. J.; van Santen, R. A. *Phys. Rev. Lett.* **1990**, *64*, 1955–1958.
- (55) MacKerell, A. D.; Bashford, D.; Bellott, M.; Dunbrack, R. L.; Evanseck, J. D.; Field, M. J.; Fischer, S.; Gao, J.; Guo, H.; Ha, S.; Joseph-McCarthy, D.; Kuchnir, L.; Kuczera, K.; Lau, F. T. K.; Mattos, C.; Michnick, S.; Ngo, T.; Nguyen, D. T.; Prodhom, B.; Reiher, W. E.; Roux, B.; Schlenkrich, M.; Smith, J. C.; Stote, R.; Straub, J.; Watanabe, M.; Wiorkiewicz-Kuczera, J.; Yin, D.; Karplus, M. *J. Phys. Chem. B* **1998**, *102*, 3586–3616.
- (56) Jorgensen, W. L.; Chandrasekhar, J.; Madura, J. D.; Impey, R. W.; Klein, M. L. *J. Chem. Phys.* **1983**, *79*, 926–935.
- (57) Grubmüller, H.; Heller, H.; Windemuth, A.; Schulten, K. *Mol. Simul.* **1991**, *6*, 121–142.
- (58) Schlick, T.; Skeel, R. D.; Brunger, A. T.; Kalé, L. V.; Board, J. A.; Hermans, J.; Schulten, K. *J. Comput. Phys.* **1999**, *151*, 9–48.
- (59) Martyna, G. J.; Tobias, D. J.; Klein, M. L. *J. Chem. Phys.* **1994**, *101*, 4177–4189.
- (60) Sotomayor, M.; Vasquez, V.; Perozo, E.; Schulten, K. *Biophys. J.* **2007**, *92*, 886–902.
- (61) Mathé, J.; Aksimentiev, A.; Nelson, D. R.; Schulten, K.; Meller, A. *Proc. Natl. Acad. Sci. U.S.A.* **2005**, *102*, 12377–12382.
- (62) Heng, J. B.; Aksimentiev, A.; Ho, C.; Marks, P.; Grinkova, Y. V.; Sliger, S.; Schulten, K.; Timp, G. *Biophys. J.* **2006**, *90*, 1098–1106.
- (63) Essmann, U.; Perera, L.; Berkowitz, M. L.; Darden, T.; Lee, H.; Pedersen, L. G. *J. Chem. Phys.* **1995**, *103*, 8577–8593.
- (64) Aksimentiev, A.; Schulten, K. *Biophys. J.* **2005**, *88*, 3745–3761.
- (65) NAMD-Energy is a VMD plugin that provides both a graphical user interface and text commands for evaluating energies using NAMD. URL: <http://www.ks.uiuc.edu/Research/vmd/plugins/namdenergy/>.
- (66) Beckstein, O.; Tai, K.; Sansom, M. S. P. *J. Am. Chem. Soc.* **2004**, *126*, 14694–14695.
- (67) Qiao, R.; Aluru, N. R. *J. Chem. Phys.* **2003**, *118*, 4692–4701.
- (68) Heng, J. B.; Aksimentiev, A.; Ho, C.; Marks, P.; Grinkova, Y. V.; Sliger, S.; Schulten, K.; Timp, G. *Nano Lett.* **2005**, *5*, 1883–1888.
- (69) Chen, P.; Mitsui, T.; Farmer, D. B.; Golovchenko, J.; Gordon, R. G.; Branton, D. *Nano Lett.* **2004**, *4*, 1333–1337.
- (70) Wei, C.; Bard, A. J.; Feldberg, S. W. *Anal. Chem.* **1997**, *69*, 4627–4633.
- (71) Wang, C.; Kuzuu, N.; Tamai, Y. *J. Non-Cryst. Solids* **2003**, *318*, 131–141.
- (72) Maranas, J. K.; Chen, Y.; Stillinger, D. K.; Stillinger, F. H. *J. Chem. Phys.* **2001**, *115*, 6578–6589.
- (73) Skuja, L. *J. Non-Cryst. Solids* **1998**, *239*, 16–48.
- (74) Lee, J. W.; Tomozawa, M.; MacCrone, R. K. *J. Non-Cryst. Solids* **2008**, *354*, 1509–1515.
- (75) Fitting, H. J.; Barfels, T.; von Czarnowski, A.; Trukhin, A. N. *Mater. Sci. Eng., B* **2000**, *71*, 109–114.
- (76) Moritani, K.; Teraoka, Y.; Takagi, I.; Moriyama, H. *Nucl. Instrum. Methods Phys. Res., Sect. B* **2005**, *232*, 317–321.
- (77) Roux, B. *Acc. Chem. Res.* **2002**, *35*, 366–375.
- (78) Patra, M.; Karttunen, M. *J. Comput. Chem.* **2004**, *25*, 678–689.